

Mechanisms contributing to synaptic Ca^{2+} signals and their heterogeneity in hair cells

Thomas Frank^{a,b}, Darina Khimich^a, Andreas Neef^c, and Tobias Moser^{a,b,c,1}

^aInnerEarLab, Department of Otolaryngology and Center for Molecular Physiology of the Brain, University of Göttingen, 37099 Göttingen, Germany;

^bInternational Max Planck Research School for Neurosciences, Göttingen Graduate School for Neuroscience and Molecular Biosciences, 37077 Göttingen, Germany; and ^cBernstein Center for Computational Neuroscience, University of Göttingen, 37073 Göttingen, Germany

Communicated by A. James Hudspeth, The Rockefeller University, New York, NY, December 25, 2008 (received for review October 30, 2008)

Sound coding at hair cell ribbon synapses is tightly regulated by Ca^{2+} . Here, we used patch-clamp, fast confocal Ca^{2+} imaging and modeling to characterize synaptic Ca^{2+} signaling in cochlear inner hair cells (IHCs) of hearing mice. Submicrometer fluorescence hotspots built up and collapsed at the base of IHCs within a few milliseconds of stimulus onset and cessation. They most likely represented Ca^{2+} microdomains arising from synaptic Ca^{2+} influx through $\text{Cav}1.3$ channels. Synaptic Ca^{2+} microdomains varied substantially in amplitude and voltage dependence even within single IHCs. Testing putative mechanisms for the heterogeneity of Ca^{2+} signaling, we found the amplitude variability unchanged when blocking mitochondrial Ca^{2+} uptake or Ca^{2+} -induced Ca^{2+} release, buffering cytosolic Ca^{2+} by millimolar concentrations of EGTA, or elevating the Ca^{2+} channel open probability by the dihydropyridine agonist BayK8644. However, we observed substantial variability also for the fluorescence of immunolabeled $\text{Cav}1.3$ Ca^{2+} channel clusters. Moreover, the Ca^{2+} microdomain amplitude correlated positively with the size of the corresponding synaptic ribbon. Ribbon size, previously suggested to scale with the number of synaptic Ca^{2+} channels, was approximated by using fluorescent peptide labeling. We propose that IHCs adjust the number and the gating of $\text{Cav}1.3$ channels at their active zones to diversify their transmitter release rates.

calcium microdomain | coding | imaging | ribbon synapse | modeling

Hair cells transform mechanical stimuli into glutamate release at their ribbon-type synapses (reviewed in refs. 1 and 2). This involves a tight regulation of synaptic vesicle exocytosis by Ca^{2+} channels (3–7), which are of $\text{Cav}1.3$ type (8). The Ca^{2+} channels cluster at the multiple active zones of hair cells (5, 9–14). Imaging of Ca^{2+} indicator fluorescence has revealed localized microdomains of elevated $[\text{Ca}^{2+}]_i$ in lower vertebrate hair cells (10–12, 14), whereas a spatially less confined rise of submembrane $[\text{Ca}^{2+}]_i$ involving Ca^{2+} -induced Ca^{2+} release (CICR) has been reported for immature mouse inner hair cells (IHCs) (15).

Our understanding of sound encoding in the mammalian cochlea is partly limited by a lack of quantitative information on synaptic Ca^{2+} signaling in the IHCs of hearing animals. For example, it is believed that differences between the synapses of an individual IHC account for the variability of spontaneous and evoked rates, sound threshold, and dynamic range among spiral ganglion neurons (SGNs) of similar characteristic frequency (16). Presynaptic and postsynaptic mechanisms have been suggested to cause this heterogeneity of SGN dynamics. Differential efferent control of SGN activity (17) seems conceptually obvious. There are also indications for differences in structure (18) and function (19) among active zones of an IHC; however, little is known about the underlying mechanism. Here, we used time-resolved confocal imaging of the fluorescence of low-affinity Ca^{2+} indicators together with pharmacological manipulations and modeling to characterize synaptic Ca^{2+} microdomains in IHCs of hearing mice.

Results

Fast and Localized Ca^{2+} Signals Mediated by Ca^{2+} Influx at IHC Active Zones. Voltage activation of Ca^{2+} influx caused the appearance of submicrometer fluorescence hotspots in the basolateral compartment of IHCs ($[\text{Ca}^{2+}]_e = 5 \text{ mM}$; Fig. 1A) that had been filled with the low-affinity Ca^{2+} indicator Fluo-5N ($400 \mu\text{M}$, $K_d = 95 \mu\text{M}$; M. Alp and W. M. Roberts, personal communication) and the slow Ca^{2+} chelator EGTA (2 mM , $K_d = 180 \text{ nM}$ at pH 7.2) (20). These conditions (“standard conditions”) favored detection of localized Ca^{2+} signals by augmenting Ca^{2+} influx (elevated $[\text{Ca}^{2+}]_e$) and limiting intracellular Ca^{2+} spread (EGTA, e.g., ref. 14). The low affinity of Fluo-5N led us to primarily display fluorescence changes ($F - F_0$ or ΔF) without background normalization (avoiding an increase in noise due to division by low F_0). In contrast to reports regarding other ribbon synapses (10), we did not observe obvious spot-like Ca^{2+} indicator fluorescence at rest, arguing against a notable association of the indicator with ribbons. The Ca^{2+} indicator fluorescence hotspots (spanning hundreds of nanometers) are further on referred to as Ca^{2+} microdomains to distinguish them from Ca^{2+} nanodomains, which are implied for Ca^{2+} signals that operate within a few tens of nanometers of the source and have escaped visualization because of the limited spatial resolution of conventional light microscopes (21).

The Ca^{2+} microdomains colocalized with synaptic active zones, shown by marking the synaptic ribbons with a rhodamine-conjugated CtBP2/RIBEYE-binding peptide (Fig. 1B) (22). We did not observe CtBP2/RIBEYE-marked spots without Ca^{2+} microdomains. We searched for Ca^{2+} microdomains in stacks of confocal sections from the base to the apex of the IHC that were acquired during repetitive depolarization. The number of Ca^{2+} microdomains (8 ± 2 per IHC, $n = 4$ IHCs) was consistent with typical observations of labeled ribbons (e.g., Figs. 1B Left and 5B). Neither Ca^{2+} microdomains nor ribbons were observed apical to the nucleus. Ca^{2+} microdomains could not be elicited in the absence of extracellular Ca^{2+} (Fig. 1C, representative for $n = 3$ IHCs).

The spatiotemporal properties and voltage dependence of synaptic Ca^{2+} microdomains were studied at high temporal resolution by using “spot detection” (23) and line scanning. For spot detection, we positioned the laser beam on the brightest pixel in a Ca^{2+} microdomain of the previously acquired xy-scan (white spot in the center of the Ca^{2+} microdomain of Fig. 2A) and recorded the fluorescence at an effective rate of $\approx 2 \text{ kHz}$ (Methods). Note that we visually chose the best focal plane, routinely performed spot detection at 7 locations in a line (standard method; white spots in Fig. 2A, enabling isochronal

Author contributions: T.F. and T.M. designed research; T.F. and D.K. performed research; T.F. and A.N. analyzed data; and T.F., A.N., and T.M. wrote the paper.

The authors declare no conflict of interest.

¹To whom correspondence should be addressed. E-mail: tmoser@gwdg.de.

This article contains supporting information online at www.pnas.org/cgi/content/full/0813213106/DCSupplemental.

© 2009 by The National Academy of Sciences of the USA

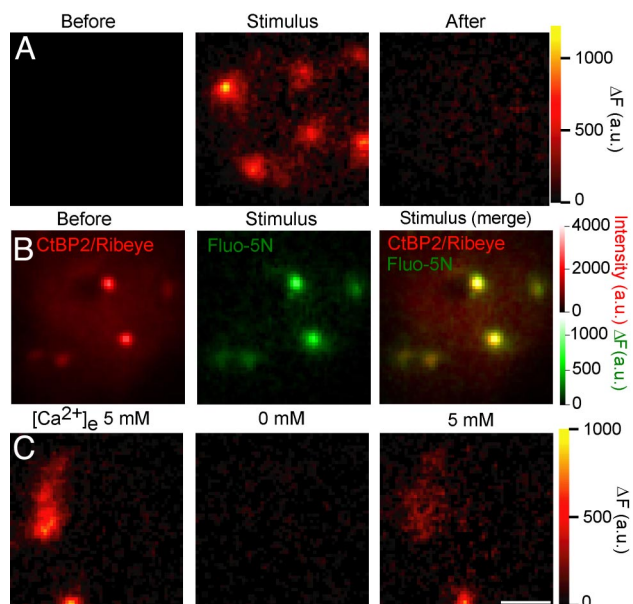


Fig. 1. Ca^{2+} microdomains mediated by Ca^{2+} influx at ribbon synapses in IHCs. Confocal images of Fluo-5N-filled IHCs were acquired in 3 repetitions of 6 images at ≈ 10 Hz: 2 images each before, during, and after stimulation by 200-ms depolarizations to -7 mV. Images averaged over runs and time frame (e.g., before stimulation) are shown. (A) Representative series of images under standard conditions showing 6 Fluo-5N fluorescence hotspots (Ca^{2+} microdomains) during the stimulus. The images were baseline subtracted (subtracting the average of the 2 images before depolarization; ΔF). On display are the image during stimulation and those preceding or following the stimulus. (B) Ca^{2+} microdomains (Center) evolved at ribbon synapses marked by rhodamine-conjugated CtBP2/RIBEYE-binding peptide (40 μM ; Left, acquired before stimulation). Overlay (Right) depicts colocalization of Ca^{2+} microdomains and synaptic ribbons (both fluorescence channels acquired simultaneously). Note the extension of Ca^{2+} microdomains beyond ribbons. For 2-dye imaging, acquisition was repeated 6 instead of 3 times. (C) Ca^{2+} microdomains were abolished by omission of extracellular Ca^{2+} (Center, bath perfusion of nominally Ca^{2+} -free solution and addition of 1 mM EGTA and 5 mM MgCl_2) and reappeared after readdition of 5 mM $[\text{Ca}^{2+}]_e$ to the IHC (imaging as in A). (Scale bars: 2 μm .)

analysis: Fig. 2C) and chose the position with the largest ΔF for further analysis.

Fig. 2B–D illustrates the rapid build-up and collapse of Fluo-5N fluorescence upon stimulus onset and cessation. We note that the presented kinetics of ΔF underestimate the true speed of the $[\text{Ca}^{2+}]$ change because of the limiting binding kinetics of the Ca^{2+} indicator as well as spatial averaging in the process of detection [supporting information (SI) Fig. S1d and SI Text] (23). The kinetics were quantified by single- or double-exponential fitting (Fig. 2B and Table S1). Moving the excitation detection volume outside the center of a given Ca^{2+} microdomain revealed a reduction of ΔF and progressive slowing of onset and offset kinetics (Fig. 2B and C). Note the pronounced amplitude variability of ΔF (Fig. 2D). The distribution of maximal ΔF values [ΔF_{max} , peak fluorescence identified after boxcar (2-ms box) smoothing] had a coefficient of variation (CV) of 0.74 (45 Ca^{2+} microdomains in 17 IHCs). Similar variance was observed in the background-normalized data ($\Delta F/F_0$, CV = 0.65; Fig. S2a) and for the ΔF_{max} distribution estimated by fitting Gaussian functions to time-averaged line scans (CV = 0.75, 35 Ca^{2+} microdomains in 17 IHCs). We observed a trend toward smaller variance with more precise colocalization of beam position and Ca^{2+} microdomain center (SI Text), probably reflecting the contribution of measurement variance. Therefore, we consider the most accurate approach (3D spot displacement) to yield the most reliable estimate of ΔF_{max} variability (CV =

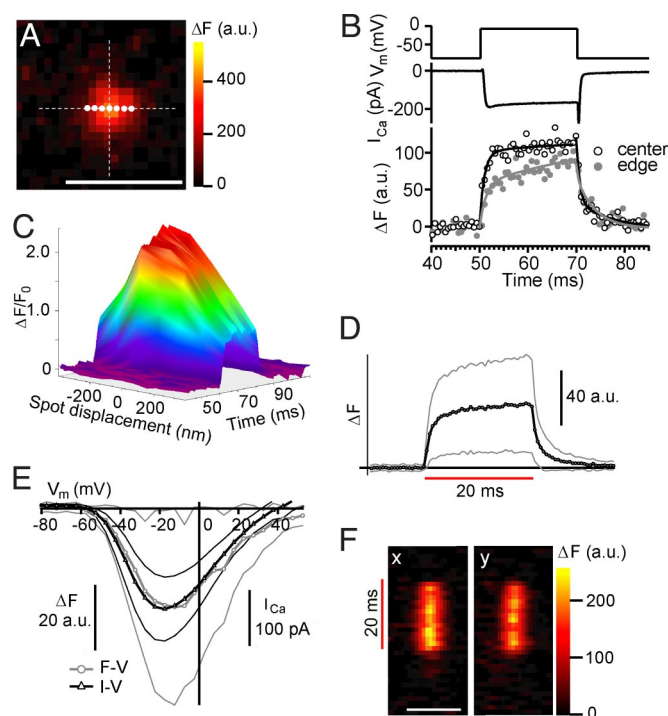


Fig. 2. Spatiotemporal properties and voltage dependence of Ca^{2+} microdomains. (A) Confocal image of a Ca^{2+} microdomain illustrating read-out sites for spot detection (white spots) and line scans (orthogonal dashed lines). (Scale bar: 2 μm .) (B) Representative spot detection experiment: the laser spot was first placed on the brightest pixel in the xy confocal image (A, center white spot). Top of the graph shows voltage protocol, middle shows Ca^{2+} current, and bottom shows ΔF at the center spot (black) and an outlying position (260 nm off center, gray). Ca^{2+} current (I_{Ca}) and ΔF represent averages obtained from 5 subsequent runs (interval: 2.25 s). Lines represent exponential fits to the ΔF rise and decay. (C) Isochronal analysis: the laser spot was subsequently displaced bilaterally from the center, and the fluorescence was recorded as described in B. ΔF traces were assembled in a pseudo-3D plot as a function of time and space. (D) Mean (black) and SD (gray) of 45 Ca^{2+} microdomains (in 17 IHCs) recorded as described in B; note the large amplitude variability. For each Ca^{2+} microdomain, only the maximum intensity recording was considered. (E) Mean and SD of ΔF (gray) as a function of depolarizing potential (V_m), obtained from spot-detection experiments at the center of the Ca^{2+} microdomain ($n = 32$ Ca^{2+} microdomains in 17 IHCs); ΔF was averaged over the last 15 ms of a 20-ms stimulus. ΔF (mean: gray) and I_{Ca} (mean: black) show a similar voltage dependence (thin lines: corresponding SDs). (F) Representative line scans (x and y, corresponding to the x and y scan lines in A). Red bar indicates time of depolarization to -7 mV. (Scale bar: 2 μm .)

0.54). However, when using this more extensive search, one trades more accuracy in beam position for more rundown of Ca^{2+} influx and risk of photodamage. Hence, we did not generally apply 3D spot displacement, but used the standard method for most experiments (unless stated otherwise).

Variability of ΔF_{max} was only slightly smaller within individual IHCs (Fig. S2 b–d and SI Text), indicating that intracellular variability dominates the variance of the entire population of Ca^{2+} microdomains. Thus, we interpret the population estimates to indicate intracellular variability throughout. Based on our in situ $F_{\text{max}}/F_{\text{min}}$ ratio (≈ 50) and noting the limitations inherent to $[\text{Ca}^{2+}]$ quantification using nonratiometric indicators, we estimated the average $[\text{Ca}^{2+}]$ within the Ca^{2+} microdomain to be ≈ 3 μM at the end of a 20-ms depolarization (standard conditions). The voltage dependence of ΔF qualitatively mimicked that of the simultaneously acquired Ca^{2+} current, further indicating that ΔF reflects synaptic Ca^{2+} influx (Fig. 2E). The spatial distribution of the Ca^{2+} signals was quantified by 2 orthogonal line scans (Fig. 2F, lines indicated in Fig. 2A). Following the Ca^{2+} microdo-

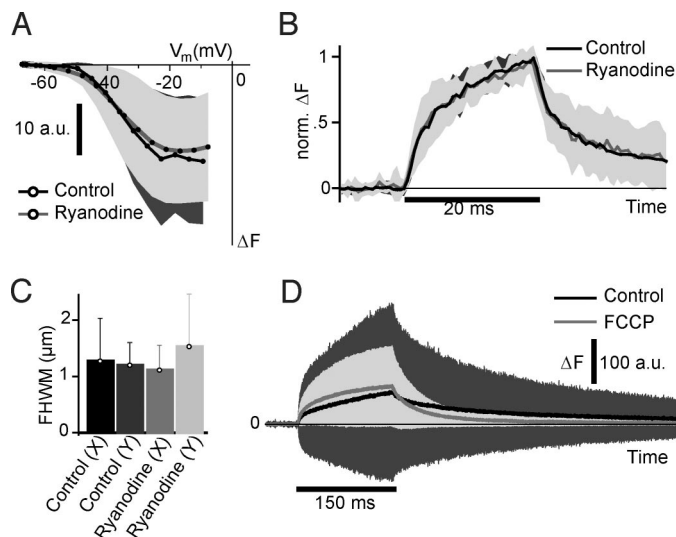


Fig. 3. Blocking CICR or mitochondrial Ca^{2+} uptake. (A) Comparable mean (line) and SD (shaded area) of ΔF vs. membrane voltage (V_m) for cells loaded with either 100 μM ryanodine (12 microdomains in 9 IHCs) or vehicle (16 microdomains in 13 IHCs) via the patch pipette (KCl-based solution with 0.5 mM EGTA; see *Methods*). ΔF was obtained by spot detection as described in Fig. 2E. For each microdomain, the voltage protocol was repeated 3 times. V_m was offline-corrected for the voltage drop over residual series resistance, which was very relevant here because of the remaining potassium current. (B) Similar onset and decay kinetics with (gray, 15 microdomains in 10 IHCs) and without (black, 19 microdomains in 14 IHCs) ryanodine. Average (line) and SD (shaded area) of normalized ΔF traces (spot detection following depolarization to “nominally” -15.3 mV; only recordings with a voltage error <4 mV were considered). (C) Mean and SD of the FWHM of the Ca^{2+} microdomain along both perpendicular scan lines (fitting of a Gaussian function to the average of all lines acquired during depolarization). No difference was found between the 2 groups. X (control): 11 Ca^{2+} microdomains in 10 IHCs, Y (control): 7 Ca^{2+} microdomains in 7 IHCs, X (ryanodine): 11 Ca^{2+} microdomains in 8 IHCs, and Y (ryanodine): 8 Ca^{2+} microdomains in 6 IHCs. (D) Mean and SD of ΔF traces recorded by spot detection in response to 150-ms depolarizations to -7 mV (0.5 mM EGTA and 375 μM Fluo-4FF in the pipette; 10 mM $[Ca^{2+}]_e$ and 5 μM BayK8644 in the bath) in control experiments ($n = 11$ Ca^{2+} microdomains in 7 IHCs), and in intracellular presence of FCCP (10 μM) and oligomycin (2.5 mg/mL), blocking mitochondrial Ca^{2+} uptake ($n = 23$ Ca^{2+} microdomains in 10 IHCs).

main build-up during the first 1–2 ms, there was little spatial spread during the course of the depolarization under standard conditions.

Exploring the Mechanisms Underlying the Ca^{2+} Microdomain Heterogeneity. What differentiates the Ca^{2+} signals between synapses of a given IHC? Possible mechanisms include disparities in Ca^{2+} release from intracellular stores (e.g., CICR), Ca^{2+} buffering, and/or Ca^{2+} sequestration. Moreover, and most importantly, there could be differences in any of the 3 determinants of Ca^{2+} influx: number of channels, open probability, and single-channel current.

CICR mediated by ryanodine receptors could amplify a Ca^{2+} influx-mediated $[Ca^{2+}]$ rise to various degrees. We tested for a potential contribution of CICR to presynaptic Ca^{2+} signals by comparing the spatiotemporal properties and the voltage dependence of the Ca^{2+} microdomains elicited by 20-ms depolarizations in the presence or absence of a ryanodine receptor antagonist (100 μM ryanodine in the pipette, Fig. 3A–C; 20 or 40 μM ryanodine in the bath, Fig. S3). To favor the detection of a small CICR contribution, we entailed weaker cytosolic Ca^{2+} buffering (0.5 mM EGTA). None of these conditions caused a significant change in ΔF (Fig. 3A and Table S1), the rise and

decay kinetics (Fig. 3B), spatial distribution (Fig. 3C), the voltage of half-maximal ΔF activation, or the variability of ΔF_{max} (Tables S1 and S2). These results are consistent with observing comparable amplitudes and amplitude scatter, regardless of whether K^+ or Cs^+ [which blocks CICR (15)] was used as the main intracellular cation. In summary, we conclude that CICR does not contribute significantly to synaptic Ca^{2+} signaling in mature IHCs and cannot explain the observed synaptic heterogeneity.

Synaptic Ca^{2+} removal may differ across IHC active zones. Ca^{2+} may be cleared temporarily by mitochondria (24) or bind to immobile cytosolic Ca^{2+} binding sites (25, 26). For sensitive detection of Ca^{2+} changes due to mitochondrial Ca^{2+} uptake, we used a Ca^{2+} indicator with higher affinity (Fluo-4FF, 375 μM , $K_d = 10$ μM ; M. Alp and W. M. Roberts, personal communication) and weak cytosolic Ca^{2+} buffering (0.5 mM EGTA). Under these conditions, blocking mitochondrial Ca^{2+} uptake by intracellular carbonyl cyanide 4-(trifluoromethoxy)phenylhydrazone (FCCP, 10 μM , coapplied with oligomycin, 2.5 mg/mL) did not alter the Ca^{2+} microdomains, except for making the slow component of the fluorescence rise slightly faster (Fig. 3D and Table S1). Moreover, the CVs of the Ca^{2+} microdomain amplitudes were in the same range (1.06 vs. 0.91 for control and FCCP, respectively), arguing against a prominent contribution of variable mitochondrial Ca^{2+} uptake to heterogeneity of synaptic Ca^{2+} signals.

Addition of EGTA (0.5, 2, and 10 mM) to the pipette solution was used to study the effects of mobile Ca^{2+} buffers on the spatiotemporal properties of Ca^{2+} microdomains and their heterogeneity in 5 mM $[Ca^{2+}]_e$. For comparison, we performed experiments under close to physiological conditions (“native” Ca^{2+} buffering, perforated-patch configuration, physiological $[Ca^{2+}]_e$: 1.3 mM). For dye loading, the perforated-patch recordings were preceded by a brief whole-cell episode (15–30 s, 2 mM $[Fluo-5N]_{pipette}$), avoiding major loss of cellular Ca^{2+} -buffering proteins (SI Text).

Spots were identified in each condition, but were of smaller amplitude and spatially more confined with higher Ca^{2+} buffering capacity (Fig. 4A–C and E). The rise and decay kinetics as well as the spatial distribution of Ca^{2+} microdomains observed in perforated-patch experiments were most similar to those found with 0.5 mM EGTA. To quantitatively characterize active-zone Ca^{2+} dynamics in the well-defined whole-cell experiments, we compared the experimental data to predictions of a model of Ca^{2+} influx, diffusion, and binding by using CalC software (27) and simulating Ca^{2+} indicator fluorescence detection (for details, see Fig. S1, SI Text, and Table S3). Mobile endogenous Ca^{2+} binding sites, which are progressively “washed out” into the pipette in the whole-cell configuration, were disregarded, as were mitochondrial Ca^{2+} uptake and CICR. ΔF was predicted by transforming the spatiotemporal distribution of Ca^{2+} -bound Fluo-5N by our in situ F_{max}/F_{min} ratio (≈ 50), as described (28), and convolution with the point spread function of the optical setup. The model predicted the mean properties of the fluorescent hotspots under the different conditions reasonably well (Fig. 4C–E).

Experiments and model consistently showed biexponential rise and decay kinetics in weak exogenous buffering conditions, whereas the slow components were strongly diminished by increasing EGTA (Fig. 4D and Table S1). In addition, high EGTA accelerated the fast Ca^{2+} decay (Fig. 4D and Table S1). The widths of the Ca^{2+} microdomains in different EGTA concentrations were well predicted by the model (Fig. 4E). The width of the Ca^{2+} microdomains increased throughout the depolarization (20 ms) for lower concentrations, but it rapidly reached steady state with EGTA 2 mM or greater (Fig. S4). The choice of the Ca^{2+} -buffering condition did not appreciably affect the experimentally observed synaptic heterogeneity for any of the quantified parameters (Fig. 4B and Table S1). Finding

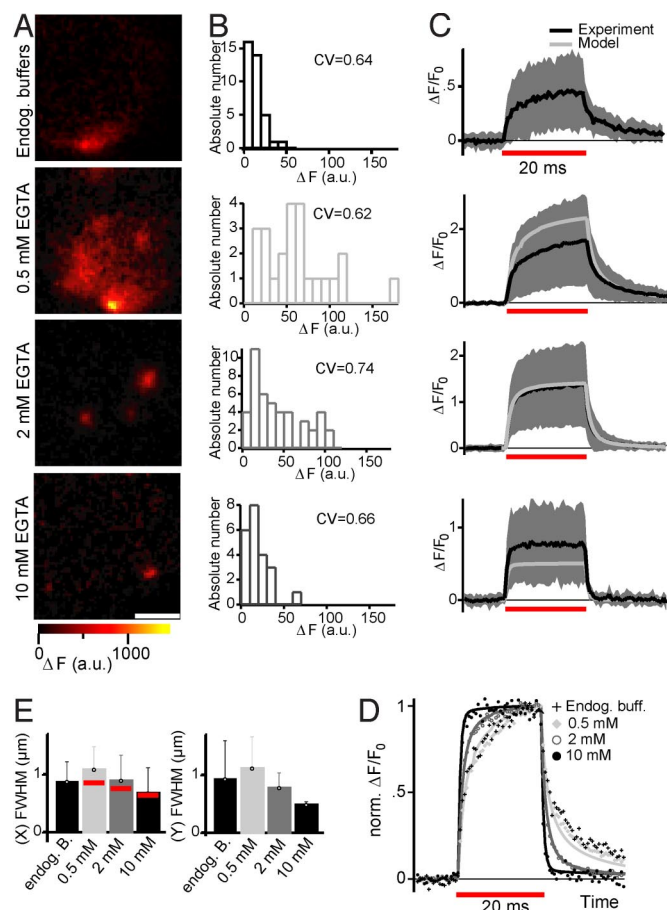


Fig. 4. Effects of Ca^{2+} buffering on IHC Ca^{2+} microdomains. (A) Representative confocal ΔF images of IHCs (recorded as introduced in Fig. 1A) with close to native endogenous Ca^{2+} buffering (perforated-patch, top row, representing 37 Ca^{2+} microdomains in 14 IHCs) or various amounts of exogenously added EGTA: 0.5 mM (second row, representing 24 Ca^{2+} microdomains in 15 IHCs), 2 mM (third row, representing 45 Ca^{2+} microdomains in 17 IHCs), or 10 mM (bottom row, representing 22 Ca^{2+} microdomains in 7 IHCs). (Scale bar: 2 μm .) (B) Distributions of ΔF_{max} obtained for the buffering conditions in spot-detection experiments after box-car smoothing (2-ms box). (C) Experimental mean (black line) and SD (gray area) of $\Delta F/F_0$ traces as well as model prediction (gray line) for the respective buffering conditions. Model predictions were obtained only for exogenous buffering experiments (see Table S1 and SI Text). (D) Normalized mean $\Delta F/F_0$ traces of all 4 buffering conditions (markers) emphasizing the kinetic differences, and model predictions (lines) for exogenous buffering experiments. (E) Mean and SD of FWHM of the Ca^{2+} microdomain along both scan lines (fitting of a Gaussian function to the time-averaged line profile). Also shown are the model predictions (red bars).

comparable synaptic heterogeneity with an excess of mobile Ca^{2+} buffer renders differences in local Ca^{2+} buffering unlikely to contribute substantially.

Heterogeneity of Ca^{2+} influx is an attractive candidate mechanism, under direct control of the membrane potential. Indeed, we observed substantial variability in the voltage dependence of ΔF across the Ca^{2+} microdomains (Fig. 5A), even within a given IHC (dotted lines in Fig. 5A), which probably reflected differences in gating. The variance of the voltage of half-maximal activation was larger for the Ca^{2+} microdomains (24 mV^2 ; standard conditions, see Table S1 for other conditions) than for the Ca^{2+} current in the corresponding IHCs (5 mV^2). Voltage errors due to changes in electrode potential were found to be less than 3 mV, and series resistance-related errors were corrected offline.

However, substantial ΔF variability was observed also for

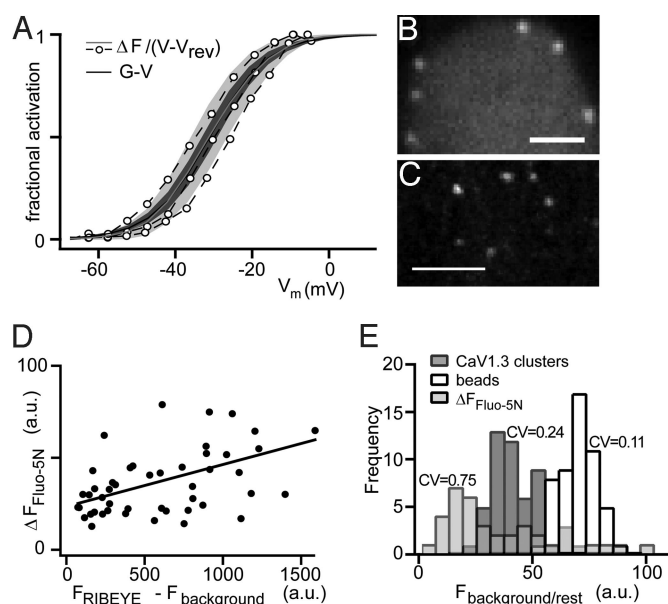


Fig. 5. Heterogeneous voltage dependence and Ca^{2+} channel number of synaptic Ca^{2+} channel clusters in IHCs. (A) To demonstrate the variable voltage dependence of ΔF_{max} , we display the average results (and SD) of fitting a Boltzmann function to the fractional voltage activation of ΔF [ΔF divided by the driving force ($V - V_{\text{rev}}$) of the underlying Ca^{2+} current]. Note that at -7 mV, the potential used for comparisons in Figs. 2D and F, 3B–D, 4, and 5D and E, the activation of ΔF (mean: gray line, SD: light gray area) and I_{Ca} (mean: black line, SD: dark gray area) is nearly complete. Note the pronounced variability in the voltage dependence of activation, even within 1 cell (dashed traces: individual data curves from 3 Ca^{2+} microdomains in an IHC). (B) shows an xy scan through the basal portion of an IHC loaded with rhodamine-conjugated, CtBP2/RIBEYE-binding peptide (40 μM ; dissolved in intracellular solution). Note the spots of increased fluorescence intensity, indicative of synaptic ribbons. (Scale bar: 2 μm .) (C) Representative confocal section of an IHC stained with a $\text{CaV}1.3$ antibody. (Scale bar: 2 μm .) (D) Correlation between Ca^{2+} microdomain ΔF_{max} and fluorescence intensity of the corresponding ribbon (amplitude of 2D Gaussian function, fit to the fluorescently tagged ribbon in xy scans acquired at rest and before spot detection). The microdomain ΔF_{max} was obtained at the maximum-intensity location, identified by a series of 11 axially (along optical axis) displaced measurements (200-nm steps). Note the positive correlation ($P_r = 0.47$, $P < 0.01$; $n = 48 F_{\text{Ca}} - F_{\text{RIBEYE}}$ pairs in 18 IHCs). (E) Distributions of Ca^{2+} microdomain ΔF_{max} (amplitude of 1D Gaussian fit to time-averaged line-scan profile, $n = 35$), $\text{CaV}1.3$ immunofluorescence ($n = 50$), and 210-nm crimson bead fluorescence ($n = 52$).

saturation stimuli (at -7 mV: Fig. 5A; see Figs. 2, 4, and 5 for illustration). Next, we tested whether the dihydropyridine L-type channel agonist BayK8644 (29) could reduce the ΔF heterogeneity of the Ca^{2+} microdomains. By uniformly increasing the open probability of $\text{CaV}1.3$ channels in IHCs (5), we reasoned that BayK8644 would equalize stimulus-dependent Ca^{2+} influx between IHC active zones. To prevent local Ca^{2+} saturation of Fluo-5N, we added a high concentration of EGTA (10 mM in the pipette, shown above to not reduce heterogeneity of ΔF). However, despite the maximized open probability, we still found large variability in ΔF ($\text{CV} = 0.87$, 16 Ca^{2+} microdomains in 5 IHCs) (Table S1).

The Ca^{2+} channel number per active zone has been suggested to vary with the size of the synaptic ribbon in hair cells in chick, frog, and turtle hair cells (30). This was based on a correlation of the estimates of Ca^{2+} channel number and of total release area (product of synapse number and ribbon size) per hair cell. Here, we explored this hypothesis at the single-synapse level and asked whether differences in channel number could contribute to the heterogeneity of Ca^{2+} microdomain amplitudes. We related the Ca^{2+} microdomain amplitude (Fluo-5N ΔF , spot detection,

20-ms depolarizations to -7 mV) to the fluorescence intensity of the corresponding peptide-labeled ribbons before depolarization (Fig. 1*B* and 5*B*). Ribbon fluorescence intensity (amplitude of 2D Gaussian function fit) rather than FWHM was used for approximation of ribbon size, because ribbons are too small to be faithfully measured by confocal microscopy (31). Relating the fluorescence intensity to ribbon size seems reasonable, as previous work (22) indicated a quantitative scaling of ribbon labeling by the fluorescent CtBP2/RIBEYE-binding peptide with the number of contained RIBEYE molecules. As shown in Fig. 5*D*, we did observe a significant correlation between Ca^{2+} microdomain amplitude and the ribbon fluorescence intensity. This suggests that larger Ca^{2+} microdomain amplitudes arose from bigger active zones, probably containing more Ca^{2+} channels, and that differences in Ca^{2+} channel number among synapses can account for part of the variance of their Ca^{2+} microdomain amplitudes.

The attractive hypothesis of a variable Ca^{2+} channel content was tested by confocal microscopy of active zones following $\text{Ca}_v1.3$ immunolabeling (Fig. 5*C*). We estimated the fluorescence intensity as described above for ribbons. Images were acquired using a low numerical aperture (0.7) objective lens to ensure that most of the $\text{Ca}_v1.3$ immunofluorescent spot was included in the excitation-detection volume. We reasoned that active zones with larger Ca^{2+} channel clusters or clusters with higher Ca^{2+} channel densities would display higher fluorescence intensities (assuming a linear labeling reaction). The measurement revealed considerable variance among the synapses ($\text{CV} = 0.24$; Fig. 5*E*). We also measured fluorescent beads using the same microscope and detection settings (diameter 210 nm; Fig. 5*E*) to get an upper boundary of the imaging- and analysis-related contributions ($\text{CV} = 0.11$). For comparison, Fig. 5*E* also displays the fluorescence intensity distribution of Fluo-5N hotspots.

Discussion

Toward a Quantitative Understanding of the Active-Zone Ca^{2+} Microdomain in IHCs. Studying IHCs of mice after the onset of hearing (low-affinity Ca^{2+} indicator, 0.5–10 mM EGTA), we observed spatially confined Ca^{2+} domains much like those reported for lower vertebrate hair cells (10–12, 14). Based on our experiments, localized domains of high Ca^{2+} concentration are likely to occur at IHC synapses with physiological Ca^{2+} influx and native Ca^{2+} buffering. Several lines of evidence suggest that the observed Ca^{2+} microdomains arose from Ca^{2+} influx through synaptic $\text{Ca}_v1.3$ Ca^{2+} channel clusters at the ribbon synapses. First, they occurred at sites marked by a ribbon-labeling, CtBP2/RIBEYE-binding, fluorescent peptide, and their number was consistent with counts of ribbon synapses (this study, and ref. 31). This argues against an appreciable fraction of presynaptically silent synapses as well as against Ca^{2+} microdomains occurring outside ribbon-type active zones. Second, Ca^{2+} microdomains were not observed when removing extracellular Ca^{2+} . Third, their amplitude shared the voltage dependence of the whole-cell Ca^{2+} current. Fourth, inhibition of CICR by ryanodine or intracellular Cs^+ did not reduce the amplitude of the Ca^{2+} microdomains. Finally, the fluorescence changes could be reasonably well predicted by realistic modeling of active-zone Ca^{2+} signals, driven solely by Ca^{2+} influx, without invoking additional Ca^{2+} sources.

Experiments with different EGTA concentrations and modeling were used to explore how mobile Ca^{2+} buffering shapes the spatiotemporal properties of the Ca^{2+} microdomains. In brief, the more mobile Ca^{2+} binding sites were present, the faster, smaller, and spatially more constrained were the observed and simulated Ca^{2+} changes. This can be intuitively understood to reflect a faster Ca^{2+} capturing and less Ca^{2+} buffer saturation. Mobile Ca^{2+} buffering presented the prevailing Ca^{2+} removal

mechanism, limiting the active zone's Ca^{2+} signal of IHCs in space and time during short depolarizations. This agrees well with conclusions of previous studies on other hair cells (11, 12).

Heterogeneity of Synaptic Ca^{2+} Signals: Mechanisms and Consequences. The voltage dependence varies even among active zones of an individual IHC, which may relate to the observation of different stimulus thresholds for styryl dye destaining across putative ribbon synapses (19). Because the hair cell is isopotential (9), voltage errors due to series resistance were corrected, and those due to drifts in electrode potential were minor, we expect experimental procedures to contribute little to the observed variance of the voltage of half activation (24 mV^2), which was 4 times larger than that of the whole-cell current compared among the same experiments.

Besides shifts in activation curves, we also found a large ΔF_{max} variability of Ca^{2+} microdomains for strong depolarizations (-7 mV) when Ca^{2+} channel activation saturates and even after maximization of channel open probability by BayK8644. Although some contribution of the measurement to the observed variance of Ca^{2+} microdomain amplitude is likely, this indicates variability of Ca^{2+} signaling in addition to that arising from differences in voltage gating (discussed above). Our data do not support a major contribution of Ca^{2+} signal amplification by CICR, local differences in Ca^{2+} buffering/sequestration, or the average maximal Ca^{2+} channel open probability among IHC synapses.

Heterogeneity in the number of Ca^{2+} channels among hair cell active zones could explain a substantial part of the observed amplitude variability of Ca^{2+} microdomains at saturating depolarizations. Confocal microscopy of immunolabeled $\text{Ca}_v1.3$ channel clusters indicates that the number of Ca^{2+} channels indeed varies among hair cell synapses ($\text{CV} = 0.24$; Fig. 5). This result was obtained from measurements on fixed tissue, and therefore not from those synapses that had been functionally characterized. However, the argument is supported by the simultaneous imaging of Ca^{2+} microdomains and their corresponding, fluorescently labeled ribbons. The observed positive correlation of both fluorescence intensities suggests that larger Ca^{2+} microdomains arise from active zones with more Ca^{2+} channels. This hypothesis assumes that (i) the fluorescence of the peptide-labeled ribbon indicates the number of RIBEYE molecules (22) and (ii) can be used to approximate ribbon size, (iii) which scales with the spatial extent of the active zone and the number of Ca^{2+} channels (30). Modeling confirmed that under our experimental conditions, the contributions of individual Ca^{2+} channels at the active zone sum roughly linearly to set the amplitude of the Ca^{2+} microdomain reported by the low-affinity indicator Fluo-5N and our imaging system (Fig. S1*e* and S1*Text*). Whether the remaining mismatch of amplitude variance between Ca^{2+} microdomain and $\text{Ca}_v1.3$ channel immunofluorescence reflects differences in Ca^{2+} channel regulation among synapses remains to be addressed in future studies.

In summary, we propose that the IHC adjusts both the number of Ca^{2+} channels and their gating at its individual synapses. This could explain the coexistence of synapses within an individual hair cell that drive different SGN firing rates. Transmitter release from IHCs seems to be controlled by Ca^{2+} nanodomains around Ca^{2+} channels within few tens of nanometers of the docked vesicle (2, 5, 7, 32). In this case, the number of open channels would relate linearly to the rate of vesicle exocytosis. This concept has been primarily tested for fusion of the readily releasable pool of vesicles (5, 7), but probably also applies during longer stimuli (6). Differences in the number of channels opening for given receptor potential amplitude would translate into different peak and adapted firing rates. However, synapses with more Ca^{2+} channels and/or a more negative voltage range of channel activation would also cause higher spontaneous firing rates, which in SGNs seem entirely driven by hair cell transmitter release (33). The question of how these

properties are differentially regulated in a single IHC remains to be addressed in future studies.

Methods

Animals. C57BL/6 mice (ages 14–18 days) were used for experiments.

Patch-Clamp and Confocal Ca^{2+} Imaging. IHCs from apical coils of freshly dissected organs of Corti were patch-clamped as described previously (4). The pipette solution contained (in mM): 130 cesium glutamate, 13 tetraethylammonium (TEA)-Cl, 20 CsOH-Hepes, and 1 MgCl_2 , and 250 $\mu\text{g/mL}$ amphotericin B (pH 7.2) for perforated-patch recordings, in addition to (in mM) 2 MgATP, 0.3 NaGTP, and various concentrations of EGTA (standard: 2 mM; cesium glutamate concentration adjusted for 10 mM EGTA), 0.4 mM Fluo-5N or 0.375 mM Fluo-4FF (penta- K^+ salts; Invitrogen) (pH 7.0) for standard whole-cell recordings, and for CICR experiments (in mM): 155 KCl, 20 KOH-Hepes, 2 MgATP, and 0.3 NaGTP (pH 7.0). The extracellular solution contained (in mM; if deviating, concentrations used for CICR experiments are given in brackets): 102 [133] NaCl, 35 [3] TEA-Cl, 2.8 [5.8] KCl, 5 CaCl_2 (1.3 for perforated-patch recordings; balanced by NaCl), 1 MgCl_2 , 10 NaOH-Hepes, and 10 D-glucose (pH 7.3). BayK8644 (5 μM ; Tocris) was bath applied. Ryanodine (Calbiochem) was either dissolved in the pipette solution (100 μM) or continuously bath applied (20 or 40 μM). FCCP (10 μM ; Fluka) and oligomycin (2.5 mg/mL; Sigma) were intracellularly applied. An EPC-9 amplifier and Patchmaster software (HEKA Elektronik) were used for measurements. All voltages were corrected for liquid-junction potentials (17.5 mV for cesium glutamate solution and 5.3 mV for KCl solution) and voltage drops across series resistance. Currents were low-pass-filtered at 5 kHz and sampled at 50 kHz. Cells with a membrane current exceeding -50 pA at our standard holding potential of -87.5 mV (cesium glutamate; for KCl solution, -75.3 mV) were discarded from analysis. Ca^{2+} currents were further isolated from background current by using a P/n protocol. Current-voltage relationships were fitted by using a Boltzmann function. Interstimulus periods were 2–3 s between sweeps and 1–2 min between ensembles. The average Ca^{2+} current rundown at the end of the experiment was 30% of the maximum current.

Ca^{2+} imaging was performed with a Fluoview 300 confocal scanner mounted on an upright microscope (BX50WI) equipped with a 0.9 numerical aperture, 60 \times water-immersion objective (all from Olympus). A 50-mW, 488-nm laser (Cyan; Newport Spectraphysics) was used for excitation of Fluo-5N, and a 1.5-mW, 543-nm He-Ne laser was used for excitation of rhodamine-conjugated, CtBP2/RIBEYE-binding peptide. Ca^{2+} microdomains were identi-

fied in xy scans during 200-ms depolarizations [0.5% of maximum laser intensity (488 nm)] and were further characterized by using spot detection and line scans. During spot detection [0.05% of maximum laser intensity (488 nm)], the output of the photomultiplier tube (PMT) signal (500 kHz) was temporally averaged to yield an effective sampling rate of 1.85 kHz. Line scans were acquired at a rate of 0.74 kHz [0.25% of max laser intensity (488 nm)]. Isochronal spot detection measurements and line scans were repeated 5 and 10 times, respectively. For 2-dye imaging, the laser intensities (488 nm) were doubled. The 543-nm laser was operated at the following intensities: 50% for xyscans, 25% for line scans, and 10% for spot detection. PMT dark current was subtracted for all measurements, and PMT settings were identical for all experiments. In rare cases, we observed an unclear long-term rise in fluorescence that was independent of leak current amplitude.

Immunohistochemistry. The freshly dissected apical cochlear turns were fixed for 25 min in 99% methanol at -20°C . Immunostaining was performed as described in ref. 31. The following antibodies were used: mouse IgG1 anti-CtBP2 (also recognizing the ribbon protein RIBEYE; 1:150; BD Biosciences), rabbit-anti- $\text{Ca}_v1.3$ (1:75; Alomone Labs), and secondary AlexaFluor488-labeled and AlexaFluor568-labeled antibodies (1:200; Molecular Probes). Confocal images of $\text{Ca}_v1.3$ -immunolabeled IHCs were acquired by using an SP5 confocal microscope (Leica) with 488-nm (Ar) and 561-nm (DPSS) lasers for excitation and a 63 \times oil immersion objective (numerical aperture 0.7).

Model and Data Analysis. Fig. S1, S1 Text, and Table S3 provide a detailed description of the model using CalC (<http://web.njit.edu/~matveev/calc.html>). Data are presented as mean and SD. Igor Pro 6 (Wavemetrics) was used for analysis.

ACKNOWLEDGMENTS. We thank A. Egner for contribution to the $\text{Ca}_v1.3$ immunofluorescence imaging; V. Matveev for providing CalC simulation software; D. Zenisek and G. Matthews for providing fluorescently labeled CtBP2/RIBEYE-binding peptide; F. Wolf and E. Neher for discussion; and E. Neher, F. Wolf, A. Lee, N.M. Chapochnikov, and T. Sakaba for their comments on the manuscript. This work was supported by a Lichtenberg Fellowship of the state of Lower Saxony (to T.F.) and grants from the Deutsche Forschungsgemeinschaft, Center for Molecular Physiology of the Brain, the Human Frontier Science Program (to T.M.), the European Commission (EuroHear; to T.M.), the Max Planck Society (tandem project, to T.M.), and the Federal Department for Education and Research (Bernstein Center for Computational Neuroscience Goettingen to T.M. and Bernstein fellowship to A.N.).

- Fuchs PA, Glowatzki E, Moser T (2003) The afferent synapse of cochlear hair cells. *Curr Opin Neurobiol* 13:452–458.
- Moser T, Neef A, Khimich D (2006) Mechanisms underlying the temporal precision of sound coding at the inner hair cell ribbon synapse. *J Physiol* 576:55–62.
- Parsons TD, Lenzi D, Almers W, Roberts WM (1994) Calcium-triggered exocytosis and endocytosis in an isolated presynaptic cell: Capacitance measurements in saccular hair cells. *Neuron* 13:875–883.
- Moser T, Beutner D (2000) Kinetics of exocytosis and endocytosis at the cochlear inner hair cell afferent synapse of the mouse. *Proc Natl Acad Sci USA* 97:883–888.
- Brandt A, Khimich D, Moser T (2005) Few $\text{Ca}_v1.3$ channels regulate the exocytosis of a synaptic vesicle at the hair cell ribbon synapse. *J Neurosci* 25:11577–11585.
- Keen EC, Hudspeth AJ (2006) Transfer characteristics of the hair cell's afferent synapse. *Proc Natl Acad Sci USA* 103:5537–5542.
- Goutman JD, Glowatzki E (2007) Time course and calcium dependence of transmitter release at a single ribbon synapse. *Proc Natl Acad Sci USA* 104:16341–16346.
- Platzter J, et al. (2000) Congenital deafness and sinoatrial node dysfunction in mice lacking class D L-type Ca^{2+} channels. *Cell* 102:89–97.
- Roberts WM, Jacobs RA, Hudspeth AJ (1990) Colocalization of ion channels involved in frequency selectivity and synaptic transmission at presynaptic active zones of hair cells. *J Neurosci* 10:3664–3684.
- Issa NP, Hudspeth AJ (1994) Clustering of Ca^{2+} channels and Ca^{2+} -activated K^+ channels at fluorescently labeled presynaptic active zones of hair cells. *Proc Natl Acad Sci USA* 91:7578–7582.
- Tucker T, Fettiplace R (1995) Confocal imaging of calcium microdomains and calcium extrusion in turtle hair cells. *Neuron* 15:1323–1335.
- Issa NP, Hudspeth AJ (1996) The entry and clearance of Ca^{2+} at individual presynaptic active zones of hair cells from the bullfrog's sacculus. *Proc Natl Acad Sci USA* 93:9527–9532.
- Rodriguez-Contreras A, Yamoah EN (2001) Direct measurement of single-channel Ca^{2+} currents in bullfrog hair cells reveals two distinct channel subtypes. *J Physiol* 534:669–689.
- Zenisek D, Davila V, Wan L, Almers W (2003) Imaging calcium entry sites and ribbon structures in two presynaptic cells. *J Neurosci* 23:2538–2548.
- Kennedy HJ, Meech RW (2002) Fast Ca^{2+} signals at the mouse inner hair cell synapse: A role for Ca^{2+} induced Ca^{2+} release. *J Physiol* 539:15–23.
- Liberman MC (1980) Morphological differences among radial afferent fibers in the cat cochlea: An electron-microscopic study of serial sections. *Hear Res* 3:45–63.
- Ruel J, et al. (2001) Dopamine inhibition of auditory nerve activity in the adult mammalian cochlea. *Eur J Neurosci* 14:977–986.
- Merchan-Perez A, Liberman MC (1996) Ultrastructural differences among afferent synapses on cochlear hair cells: Correlations with spontaneous discharge rate. *J Comp Neurol* 371:208–221.
- Griesinger CB, Richards CD, Ashmore JF (2005) Fast vesicle replenishment allows indefatigable signalling at the first auditory synapse. *Nature* 435:212–215.
- Naraghi M (1997) T-jump study of calcium binding kinetics of calcium chelators. *Cell Calcium* 22:255–268.
- Neher E (1998) Vesicle pools and Ca^{2+} microdomains: New tools for understanding their roles in neurotransmitter release. *Neuron* 20:389–399.
- Zenisek D, Horst NK, Merrifield C, Sterling P, Matthews G (2004) Visualizing synaptic ribbons in the living cell. *J Neurosci* 24:9752–9759.
- DiGregorio DA, Peskoff A, Vergara JL (1999) Measurement of action potential-induced presynaptic calcium domains at a cultured neuromuscular junction. *J Neurosci* 19:7846–7859.
- Herrington J, Park YB, Babcock DF, Hille B (1996) Dominant role of mitochondria in clearance of large Ca^{2+} loads from rat adrenal chromaffin cells. *Neuron* 16:219–228.
- Zhou Z, Neher E (1993) Mobile and immobile calcium buffers in bovine adrenal chromaffin cells. *J Physiol* 469:245–273.
- Wu YC, Tucker T, Fettiplace R (1996) A theoretical study of calcium microdomains in turtle hair cells. *Biophys J* 71:2256–2275.
- Matveev V, Sherman A, Zucker RS (2002) New and corrected simulations of synaptic facilitation. *Biophys J* 83:1368–1373.
- Borst A, Abarbanel HD (2007) Relating a calcium indicator signal to the unperturbed calcium concentration time-course. *Theor Biol Med Model* 4:7.
- Brown AM, Kunze DL, Yatani A (1984) The agonist effect of dihydropyridines on Ca channels. *Nature* 311:570–572.
- Martinez-Dunst C, Michaels RL, Fuchs PA (1997) Release sites and calcium channels in hair cells of the chick's cochlea. *J Neurosci* 17:9133–9144.
- Khimich D, et al. (2005) Hair cell synaptic ribbons are essential for synchronous auditory signalling. *Nature* 434:889–894.
- Roberts WM (1994) Localization of calcium signals by a mobile calcium buffer in frog saccular hair cells. *J Neurosci* 14:3246–3262.
- Robertson D, Paki B (2002) Role of L-type Ca^{2+} channels in transmitter release from mammalian inner hair cells. II. Single-neuron activity. *J Neurophysiol* 87:2734–2740.